Monsoons, Upwelling, and the Deoxygenation of the Northwestern Indian Ocean in Response to Middle to Late Miocene Global Climatic Shifts

Paleoceanography and Paleoclimatology

RESEARCH ARTICLE
10.1029/2019PA003762

Special Section:
The Miocene: The Future of the Past

Monsoons, Upwelling, and the Deoxygenation of the Northwestern Indian Ocean in Response to Middle to Late Miocene Global Climatic Shifts

Or M. Bialik[1,2], Gerald Auer[3], Nanako O. Ogawa[3], Dick Kroon[4], Nicolas D. Waldmann[1], and Naohiko Ohkouchi[3]

[1]The Dr. Moses Strauss Department of Marine Geosciences, Charney School of Marine Sciences, University of Haifa, Haifa, Israel, [2]Now at Institute of Geology, CEN, University of Hamburg, Hamburg, Germany, [3]Research Institute for Marine Resources Utilization (Biogeochemistry Program), Japan Agency for Marine-Earth Science and Technology, Yokosuka, Japan, [4]School of GeoSciences, University of Edinburgh, Edinburgh, UK

Key Points:
- We re-evaluate the Miocene evolution of upwelling and oxygen depletion in the Western Arabian Sea, using a multiproxy approach
- We demonstrate that upwelling and oxygen depletion underwent a gradual evolution and intensification through the middle and late Miocene
- Upwelling and oxygen minimum zone state are linked to Miocene climatic shifts, apex between 11 and 9 Ma, marked by water body denitrification

Supporting Information:
- Table S1

Correspondence to:
O. M. Bialik and G. Auer,
obialik@campus.haifa.ac.il;
gerald.auer@jamstec.go.jp

Citation:
Bialik, O. M., Auer, G., Ogawa, N. O., Kroon, D., Waldmann, N. D., & Ohkouchi, N. (2020). Monsoons, upwelling, and the deoxygenation of the northwestern Indian Ocean in response to middle to late Miocene global climatic shifts. *Paleoceanography and Paleoclimatology*, *35*, e2019PA003762. https://doi.org/10.1029/2019PA003762

Received 27 AUG 2019
Accepted 8 JAN 2020
Accepted article online 3 FEB 2020

Abstract Today, upwelling along the Oman margin in the Arabian Sea is governed by the South Asian Monsoon winds. The Oman upwelling results in the formation of an oxygen minimum zone (OMZ) spanning across the Arabian Sea and large parts of the Indian Ocean. While these conditions are recorded as early as the middle Miocene (~15 Ma), the long-term dynamics of upwelling in the Arabian Sea are as of yet poorly constrained during the middle to late Miocene. Here, we use organic and inorganic proxies combined with sedimentary and paleontological records to constrain the evolution of upwelling at Ocean Drilling Program Site 722B between ~15 and ~8.7 Ma. Our record shows that Mn depletion occurred at ~14.5 Ma, likely due to regionally confined OMZ formation at that time. Biogenic silica accumulation intensified between ~12.5 and ~11 Ma. The $\delta^{15}N$ values (>6‰) provide evidence for the onset of at least intermittent denitrification between ~11 and ~9.5 Ma during the apex of the global "carbonate crash." Our data demonstrate that upwelling and OMZ intensity in the Arabian Sea were linked to the reorganization of the Indian Ocean circulation system and South Asian Monsoon during the Miocene. The initiation of these systems occurred once the regional tectonic configuration (i.e., the uplift of the Tibetan Plateau ~25 Ma and the closure of the Tethyan seaway ~20 Ma) was in place. The subsequent development of monsoonal upwelling after 14 Ma responded to latitudinal shifts in climatic belts following the progressive Miocene glaciation of Antarctica.

1. Introduction

1.1. The Indian Ocean Oxygen Minimum Zone

Today the oxygen minimum zone (OMZ) in the Arabian Sea is one of the world's most oxygen deficient marine regions that today extends at intermediate water depths between ~100 and 1,000 m (Munz et al., 2017). The OMZ results from the intense seasonal/monsoonal upwelling along the Oman Margin (Banse et al., 2014; Lewis & Luther, 2000; Morrison et al., 1999; Stramma et al., 2008; Ward et al., 2009). The upwelling cells are forced by prevailing alongshore winds along the Somali Coast, the Somali/Findlater Jets (e.g., Findlater, 1969; Schott et al., 2009; Figure 1). Upwelling along the Oman Margin and its effect on surface water cooling and productivity are also considered a good proxy for past South Asian Monsoon (SAM) variability in the region (Kroon et al., 1991; Munz et al., 2017; Murtugudde et al., 2007).

Recently, Betzler et al. (2016) linked the initiation of upwelling and resulting OMZ with the beginning of the modern monsoonal circulation at ~13 Ma, based on sedimentological and geochemical observations on the Maldives sedimentary sequence drilled by Integrated Ocean Discovery Project (IODP) Expedition 359. These authors assume a contemporary reconfiguration of Indian Ocean circulation and the beginning of upwelling in the Arabian Sea during the Serravallian. This middle Miocene inception of monsoonal upwelling agrees with work by Gupta et al. (2015) on multiple sites along the Oman margin and the Owen Ridge. These works indicate that upwelling along the Oman margin initiated several million years earlier than previously suggested (i.e., Kroon et al., 1991). Zhuang et al. (2017) reported long-term cooling of the Arabian Sea surface water temperatures since at least 14.8 Ma based on TEX_{86} data. Their study also reports a major cooling step between 11 and 10 Ma, interpreted as the initiation of the upwelling and increased productivity along the Oman Margin. However, studies utilizing nitrogen isotopes from the eastern Arabian Sea indicate no

denitrification in the region and concluded that productivity did not significantly increase prior to 3.1 Ma during the Mid-Pliocene Warm Period (Tripathi et al., 2017). Tripathi et al. (2017) thus assume that a weaker SAM must have persisted from at least ~10.2 Ma onward. Their assumption is in contradiction with Dickens and Owen (1999, 1994), who, using multiple lines of evidence, illustrate the presence of increased productivity in the Indian Ocean at least from 9 Ma and up to 5 Ma. This proposed "biogenic bloom" in the Indian Ocean was recently confirmed and is now proposed to have started even earlier (~11.2 Ma) by Lübbers et al. (2019) in the eastern Indian Ocean (Site U1446; Figure 1).

In this study, we revisit the Langhian-Tortonian sequence from ODP Site 722B, with the aim to refine the timing and forcing of Miocene upwelling initiation and OMZ expansion. We place our data into context of the current understanding of the regional tectonic and geographic setting, which according to recent evidence was in place by ~20 Ma (e.g., Bialik et al., 2019; Clift & Webb, 2018) and thus at least ~6 Ma before the detected SAM intensification (Betzler et al., 2016) and cooling in the Arabian Sea (Zhuang et al., 2017). The aim of the present study is to test the hypothesis that while "tectonic preconditioning" was necessary to allow the modern style Indian Ocean oceanic and atmospheric circulation system, global climatic changes after the MMCO controlled the evolution of monsoonal upwelling in the Arabian Sea (Zhang et al., 2014). Moreover, as these climatic and tectonic changes were gradual and stepwise, we postulate that the initiation and subsequent evolution of upwelling will likely follow a similar long-term pattern and test this by examining a new multiproxy record in the context of previous studies. Furthermore, our revised biostratigraphic age model of Site 722B is able to better constrain the link between upwelling intensification, primary productivity, and the expansion of the cryosphere that began between 14.2 and 13.8 Ma (Shevenell, 2004; Tian et al., 2014). We propose that increasing latitudinal heat gradients resulted in a strengthening of zonal wind patterns in the tropics and subtropics, most notably the monsoons, in line with previous modeling data (Herold et al., 2011; Zhang et al., 2014).

2. Tectonic and Oceanographic Background

2.1. Site 722 Oceanography and Geology

The Owen Ridge is a 300-km-long, 50-km-wide feature with ~2,000 m of relief in the western Arabian Sea. It is a vast tilted slab extending along an 800-km-long strike-slip fault system. This feature appears to have formed during the late Oligocene to early Miocene (DSDP Leg 23, Shipboard Scientific Party, 1974). The sedimentary cover atop the ridge comprises of nannofossil ooze and chalk, silty clay, and minor amount of diatomite (ODP Leg 117, Shipboard Scientific Party, 1989). Analysis of modern high-resolution seismic data (Rodriguez et al., 2014) depicts the sedimentary deposition at 722B beginning with a mixed turbiditic-pelagic sequence deposited between 14 and 15 Ma. The sedimentary cover overlying the last turbiditic deposits comprises pelagic sediments. This pelagic sequence was perturbed at ~8.5 Ma by the principle uplift phase of the Owen Ridge rising the ridge above the Lysocline (Rodriguez et al., 2014).

2.2. Miocene Indian Ocean Oceanographic and Tectonic Setting

The tectonic and oceanographic reorganization related to the northern migration of Australia and Africa/Arabia during the Miocene significantly altered the exchange of deep and intermediate water to and from the Indian Ocean (Bialik et al., 2019; Groeneveld et al., 2017; Kuhnt et al., 2004). The resulting tectonic configuration enabled the establishment of a modern-style circulation pattern in the Indian Ocean (Schott et al., 2009) and formed the geographical settings for modern style monsoonal precipitation in India (Clift & Webb, 2018 and references therein) during the late early to early middle Miocene (Ivanova, 2009). At the aftermath of the middle Miocene Climate Optimum, the expansion of the Antarctic Ice Sheet during the middle Miocene Climate Transition strengthened the Antarctic Circumpolar Current. This began a progressive northward migration of southern hemisphere weather patterns (Groeneveld et al., 2017; Shevenell, 2004). These southern hemisphere changes are intrinsically linked to the establishment of the modern SAM (Xue et al., 2004) by controlling annual migration of the Intertropical Convergence Zone (ITCZ; Gadgil, 2018; Sirocko et al., 1996; Zhisheng et al., 2011; Figure 1). Miocene tectonic and climatic changes, such as the closure of the Mediterranean, the uplift of the Himalayas, and the glaciation of Antarctica (Betzler et al., 2016; Clift & Webb, 2018; Holbourn et al., 2018), are thus considered important for constraining the inception of the upwelling system in the north-eastern Indian Ocean (Arabian Sea) and the concomitant expansion of the OMZ (Dickens & Owen, 1994; McCreary et al., 2013).

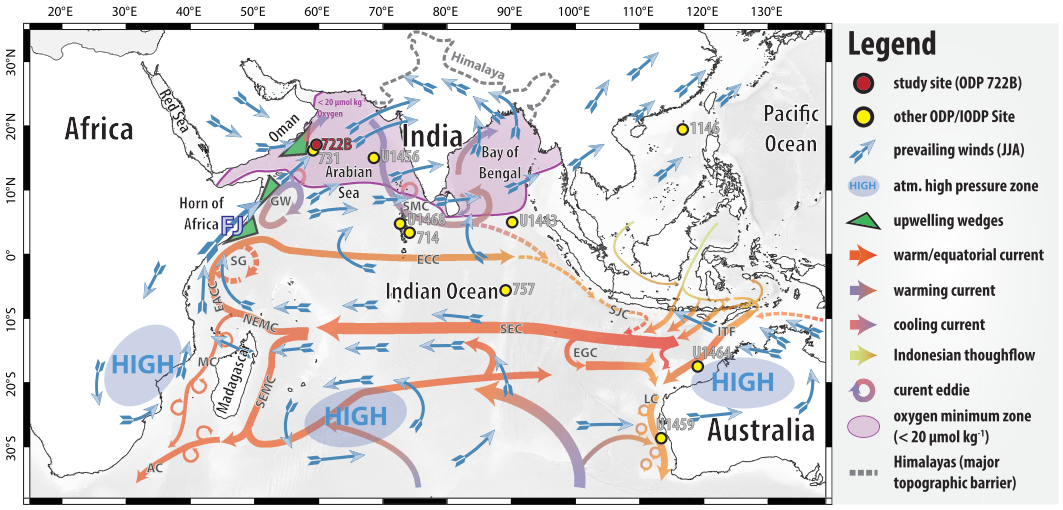

Figure 1. Map of the Indian Ocean showing the position of ODP Site 722B and reference Sites (ODP sites 714, 757, and 1146; IODP sites U1443, U1459, U1464, and U1468) in relation to the prevailing atmospheric wind (Gadgil et al., 2018; Xue et al., 2004) and oceanographic current (Schott et al., 2009) conditions during Northern Hemisphere summer (JJA). Note the southwesterly Somali/Findlater jet (FJ) along the Horn of Africa. Major Indian Ocean surface currents shown are Indonesian Throughflow (ITF), Leeuwin Current (LC), South Equatorial Current (SEC), East Gyral Current (EGC), Equatorial Counter Current (ECC), South Java Current (SJC), Agulhas Current (AC), Mosambique Current (MC), Northeast and Southeast Madagascar Current (NEMC and SEMC), Southwest Monsoon Current (SMC), Southern Gyre (SG), and Great Whirl (GW) and associated upwelling wedges (green). The present-day oxygen minimum zone in the northern Indian ocean is indicated as purple shaded area denoting oxygen concentrations <20 µmol/kg in 200-m water depth (Garcia et al., 2018; McCreary et al., 2013).

3. Materials and Methods

Original coring and analysis of Site 722 (16.6218°N/59.7953°E; Figure 1) was carried out by ODP Expedition 117 scientists aboard the JOIDES Resolution in 1987. Site 722 is located at a water depth of 2022.5 m; total recovery was 611.78 m (225.98 m in Hole A and 385.8 m in deeper Hole B, with 80.7% and 68.2% recovery, respectively). Initial sedimentological and downhole logging data were collected onboard (Shipboard Scientific Party, 1989). For sedimentological data reduction, we digitized the original shipboard Visual Description Sheets compiled by the shipboard party to define lithofacies and Munsell color index. When uncertainty regarding Visual Description Sheets content occurred, we differed to the core description in the initial report (Shipboard Scientific Party, 1989; Figure 2). Digitization of the data set was supplemented by a review of the core photos to cross verify the original description. Based on this initial data set, 71 samples were requested from the ODP core repository for further analysis using a multiproxy framework (see supporting information Table S1). These were used both in order to calibrate and corroborate the sedimentary analysis, using scanning electron microscope (SEM) imaging (Figure 3) as well as for subsequent analyses as described below.

The bulk elemental analysis was measured using a Xenemetrix S-Mobile benchtop EDS-X-Ray Fluorescence (XRF) at 28 kV over 600 mA. Samples were pressed atop an X-ray transparent thin film in Teflon containers. Spectra processing was done using CrossRoads Scientific's Fundamental Parameters software suite. All elemental data are presented in counts per second (cps) ratio form (Figure 4).

3.1. Nannofossil Biostratigraphy and Diatom Frustule Counts

For quantitative calcareous nannofossil biostratigraphy (Figure 2) and diatom frustule counts (Figure 5a) 71 samples were prepared following the methods outlined in Bordiga et al. (2015). Slides were examined using standard polarized light microscopy under 1,000X magnification. For quantitative nannofossil biostratigraphy at least two transects were counted along the short axis within the first and third third of the cover slip. Transects consist of 24 field views with 1-mm spacing. Additional transects were counted in case the minimum number of specimens was not reached. On average ~800 (median = ~600) nannofossil specimens were

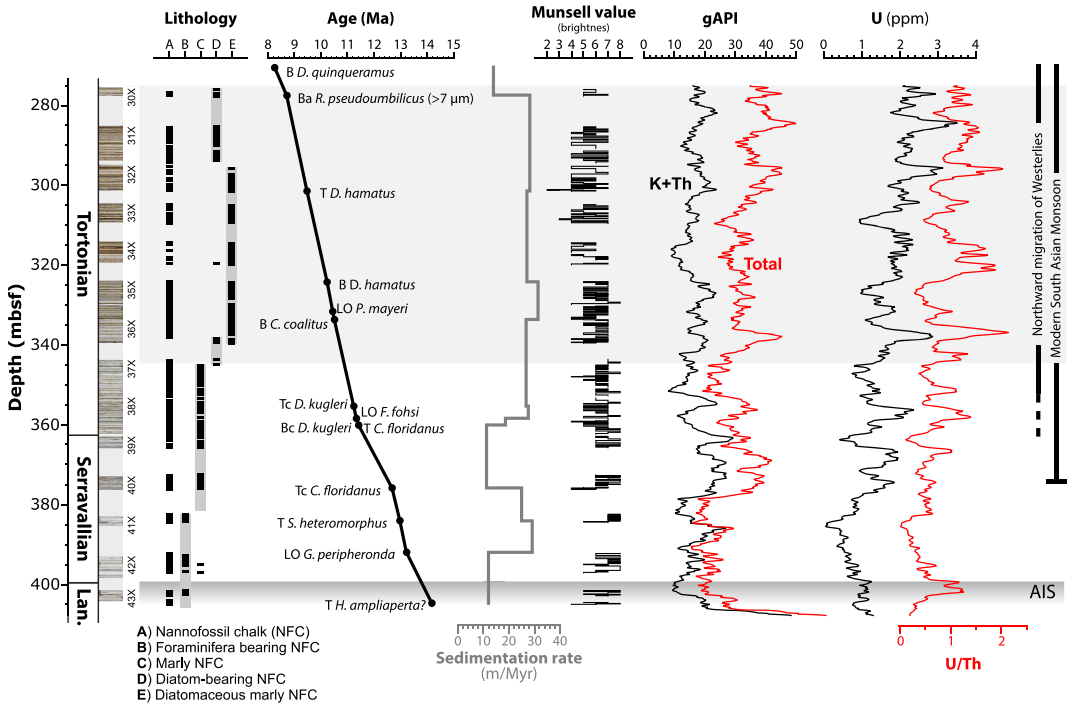

Figure 2. Lithostratigraphic and biostratigraphic data from ODP Leg 117 (Shipboard Scientific Party, 1989) in depth showing core photos, facies, updated (biostratigraphy based) age model, and sedimentation rate (see supporting information for comparision with, Munsell values (brightness), Wireline-derived total K+Th+U (=CGR; red) and K+Th (= SGR; black) gamma ray intensities, ppm U (black) derived from spectral gamma ray log, and U/Th ratio (red). Dark gray area indicates the initiation of the Antarctic Ice Sheet (AIS; Flower & Kennett, 1994), and the light gray area indicates the shift in dominant facies toward more diatomacous sediment. The timing of upwelling/OMZ initiation (Betzler et al., 2016; Gupta et al., 2015), northward migration of the Westerlies (Groeneveld et al., 2017) is indicated on the right-hand side of the figure.

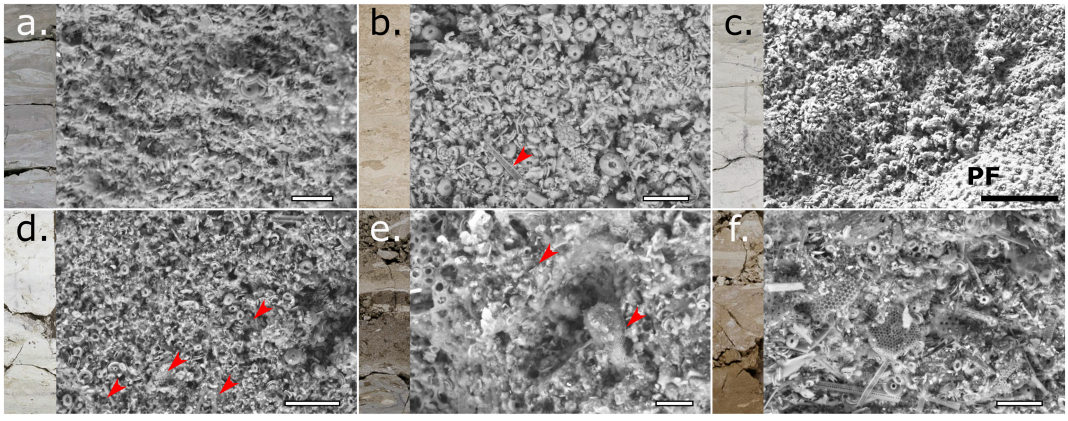

Figure 3. Principle sedimentary facies in the lower to middle Miocene of Site 722B, physical core appearance (left) and SEM images (right). (a) Nannofossil chalk (722B-40X-CCW-024); (b) Nannofossil chalk with presence of diatoms (722B-32X-02W-052); (c) Foraminifera bring nannofossil chalk (722B-42X-01W-105); (d) Marly nannofossil chalk (722B-37X-04W-09); (e) Diatom-bearing nannofossil chalk (722B-36X-CCW-032); (f) Diatomaceous marly nannofossil chalk (722B-34X-CCW035). Red arrows note locations of diatoms, PF notes location of planktonic foraminifera, white bar is 20 µm, and black bar is 50 µm; all core segment images are 20 cm in length.

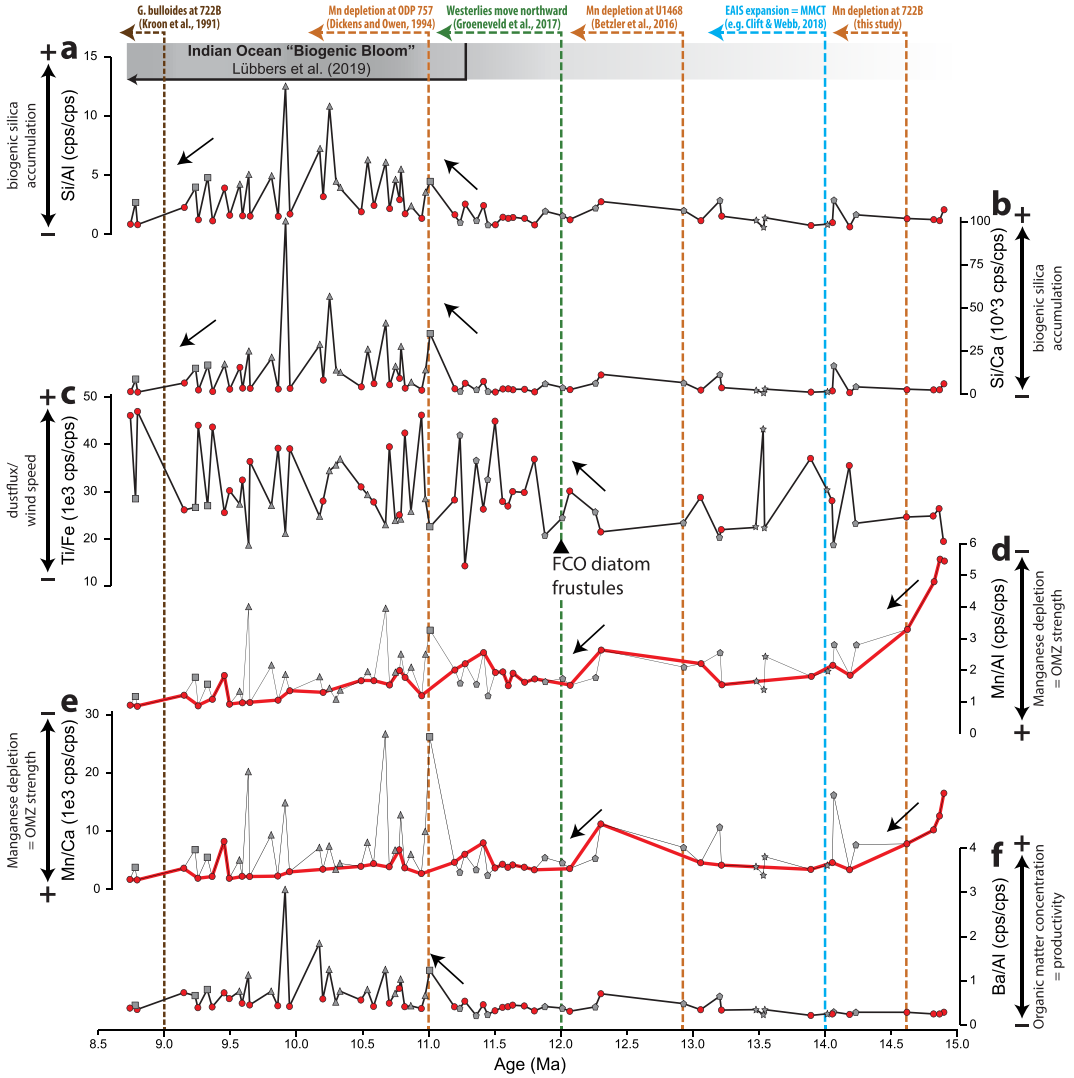

Figure 4. Elemental geochemical trends in time based on the new age model, showing XRF derived elemental ratios (cps/cps) of (a) Si/Al, (b) Si/Ca, (c) Ti/Fe, (d) Mn/Al, (e) Mn/Ca, and (f) Ba/Al. Red dots = nanofossil chalk; gray triangles = diatomaceous marly nannofossil chalk; gray cubes = diatom-bearing nannofossil chalk; gray pentagon = marly nannofossil chalk; gray stars = foraminifera-bearing nannofossil chalk. Dashed colored lines indicate major paleooceanographic and climatic events during occurring during the study interval. Shaded bar underlying the Indian Ocean "biogenic bloom" sensu Lübbers et al. (2019) reflects relative upwelling intensity along the Oman Margin with darker grays corresponding to stronger upwelling (see Figure 6).

identified per sample. Absolute number of identifications per slide depends on overall nannoplankton/diatom abundance in each sample.

Total abundance estimates of diatom frustules and stratigraphically relevant nannofossil taxa are given in number of coccoliths/frustules per gram of sedimen (N/g) (cf. Bordiga et al., 2015; supporting information Data S2).

3.2. Quantitative and Isotopic Analysis of Bulk Organic Components

All samples were analyzed for total organic carbon (TOC) content (Figure 5b). The samples were weighed, acidified using HCl to remove any carbonate material, and then the acid was evaporated. The residue was burned at 1000 °C and CO_2 discharge was measured using a Skalar Primacs SLC analyzer.

To analyze the nitrogen and organic carbon content for the C/N ratio as well as the isotopic composition of 22 samples (Figures 5c–5e), ~0.5 g of sediment was transferred to a precleaned Teflon sample vial and treated

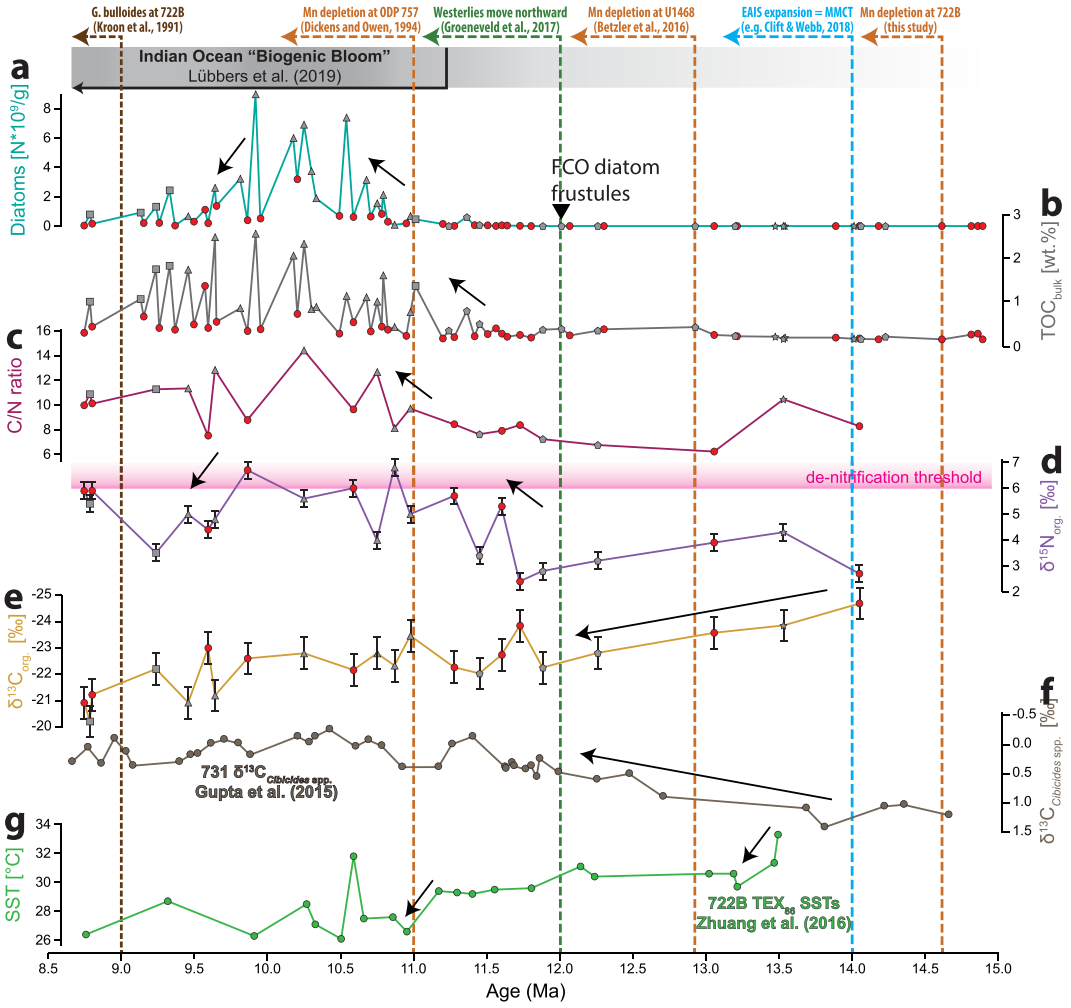

Figure 5. Primary productivity and denetrification trends at Site 722B during the middle to late Miocene. (a) Diatom abundance counts ($N*10^9/g$) as an indicator for turbulant and cold upwelling conditions. (b) Bulk sediment total organic tarbon (TOC_{bulk}) weight percent (wt. %) to show organic matter accumulation/preservation. (c) C/N ratio as an indicator for elevated paleoproductivity. (d) $\delta^{15}N$ as a proxy for N fixation and/or denetrification in oxygen depleted waters. (e) $\delta^{13}C_{org.}$ as a proxy for organic matter flux and local carbon pool depletion. (f) $\delta^{13}C_{Cibicides\ spp.}$ (Gupta et al., 2015) as a proxy for benthic $\delta^{13}C$ uptake/organic matter flux at adjacent Site 731. (g) TEX_{86}-derived sea surface temperature record of Site 722B (Zhuang et al., 2016). Red dots = nanofossil chalk; gray triangles = diatomaceous marly nannofossil chalk; gray cubes = diatom-bearing nannofossil chalk; gray pentagon = marly nannofossil chalk; gray stars = foraminifera bring nannofossil chalk. Dashed colored lines indicate major paleooceanographic and climatic events during occurring during the study interval. Shaded bar underlying the Indian Ocean "biogenic bloom" (Lübbers et al., 2019) reflects relative upwelling intensity along the Oman Margin with darker grays corresponding to stronger upwelling.

with 2 ml of 2-M ultrapure HCl. Samples were ultrasonicated for 30 min and left to rest for 5 hr before centrifugation. This step was repeated three times to ensure complete decalcification of the sample. After complete decalcification the sample was rinsed three times with Milli-Q water by adding 1.5 ml of milli-Q to each sample tube and ultrasonicated for 15 min. After centrifuging (10 min @12,000 rpm) the supernatant was removed. Rinsing was repeated at least three times or until the *p*H of the supernatant became neutral. All the samples were oven dried (~60 °C) and reground before further analysis. For analysis 2 mg of decalcified sample was measured using a sensitivity modified Flash EA 1112 coupled to a Delta plus XP IRMS through a ConFlo-III interface, Thermo Finnigan, Germany (Ogawa et al., 2010) to determine absolute carbon and nitrogen concentrations as well as their respective isotopic composition. Total C and N concentrations were obtained as weight percent relative to dried and decalcified sample weight. Isotopic ratios are presented in standard delta notation relative to atmospheric N_2 (AIR) for

Table 1
Refined Nannofossils (NF) and Planktonic Foraminifer (PF) Biostratigraphic Events at Site 722B

Depth (mbsf; shipboard data)	Depth (mbsf; this study)	Biostratigraphic event	Age (Ma)	Reference (age calibration)	Event type and comments in brackets
275.6	275.6	B *Discoaster quinqueramus*	8.3	Backman et al. (2012)	NF (shipboard)
—	277.38	B *Discoaster pentaradiatus*	8.8	Backman et al. (2012)	NF
—		Ba *Reticulofenestra pseudoumbilicus*			
290.45	290.45	FO *Neogloboquadrina acostaensis*	9.79	Wade et al. (2011)	PF; (shipboard)
305.85	301.36	T *Discoaster hamatus*	9.65	Backman et al. (2012)	NF
324.0	324.1	B *Discoaster hamatus*	10.49	Backman et al. (2012)	NF
—	333.2	T *Coccolithus miopelagicus*	10.61	Backman et al. (2012)	NF
—	333.53	B *Catinaster coalitus*	10.79	Backman et al. (2012)	NF
333.7	333.7	LO *Paragloborotalia mayeri*	10.53	Wade et al. (2011)	PF; (shipboard)
—	355.21	Tc *Discoaster kugleri*	11.6	Backman et al. (2012)	NF; (uncertain)
358.25	358.25	LO *Fohsella fohsi*	11.71	Wade et al. (2011)	PF; (shipboard)
—	359.93	T *Cylicargolithus floridanus*	11.8	Backman et al. (2012)	NF
—		Bc *Discoaster kugleri*			
—	375.68	Tc *Cyclicarolithus floridanus*	13.2	Backman et al. (2012)	NF
391.8	383.93	T *Sphenolithus heteromorphus*	13.53	Backman et al. (2012)	NF
391.8	391.8	LO *Globorotalia peripheronda*	13.8	Wade et al. (2011)	PF; (shipboard)
—	404.54	T *Helicosphaera ampliaperta*	14.86	Backman et al. (2012)	NF; (likely reworked)

Notes. Shipboard data for planktonic foraminifers were updated to numerical ages after Wade et al. (2011). Nannofossil biostratigraphc datums are based on quantitative counts from this study with ages updated to Backman et al. (2012). T = top (LO = last occurrence for PF); B = base (FO = first occurrence for PF); Tc = top common; Bc = base common; Ba = base absence (cf. Backman et al., 2012; Wade et al., 2011).

nitrogen and Vienna Pee Dee Belemnite (VPDB) for carbon (Ogawa et al., 2010). Analyses were calibrated to the BG-T (L-Tyrosine), BG-P (L-Proline), and CERKU-01 (DL-Alanine) standards (cf. Tayasu et al., 2011). Average analytical precision based on repeats using the BG-T standard was ±0.3‰ (n37) for $\delta^{15}N$ and ±0.33‰ (n38) for $\delta^{13}C$, respectively. Average precision of sample repeats was ±0.37‰ for $\delta^{15}N$, ±0.6‰ for $\delta^{13}C$, and ±0.006 wt.% for total N and ±0.1 wt.% for C.

4. Results

4.1. Refined Age Model

Nannofossil biostratigraphic datums were determined using quantitative assemblage data and total nannofossil abundance estimates based on all 71 samples. These datums were then combined with updated biostratigraphic (planktonic foraminifers and calcareous nannofossils) datums of the Hole 722B shipboard report (Shipboard Scientific Party, 1989) using astronomically calibrated absolute datums (Wade et al., 2011; Backman et al., 2012; Figure 2). Biostratigraphic information used in this study is summarized in Table 1. The age model utilizes a linear interpolation between the defined biostratigraphic datums. Based on this refined age model all events will be reported in time from here on.

4.2. Sedimentary and Wire Log Analysis

Based on the original shipboard description (Shipboard Science Party, 1989), five principle sedimentary facies were defined, all of which were corroborated by our re-evaluation (Figures 2 and 3): (1) nannofossil chalk (Figures 3a and 3b), (2) foraminifera-bearing nannofossil chalk (planktonic foraminifera mudstone to wackestone; Figure 3c), (3) marly nannofossil chalk (Figure 3d), (4) diatom-bearing nannofossil chalk (Figure 3e), and (5) diatomaceous marly nannofossil chalk (Figure 3f).

Nannofossil chalk represents the dominant facies throughout the studied core interval, with other sedimentary facies occurring as alternations (Figure 2). Between 410 and 384 mbsf (~15.3 to 13.5 Ma), these interspersed facies are primarily formed by foraminifera-bearing nannofossil chalk, although marly nannofossil chalk is also present. Between 384 and 345 mbsf (13.5 to 11.2 Ma) the intercalated facies are predominantly marly nannofossil chalk. Above 345 mbsf (11.2 Ma) intercalated facies are dominated by biogenic silica-rich intervals, either diatom-bearing nannofossil chalk (345 to 335 and above 295 mbsf, 11.2 to 10.8 and 9.4 Ma, respectively) or diatomaceous marly nannofossil chalk (335 to 295 mbsf, 10.8–9.4 Ma). As a co-occurring facies shift, siliceous fragments also begin to appear as a minor component within the nannofossil chalk facies (Figure 3b). This is noteworthy as siliceous microflora and fauna were completely

absent in this facies in the lower part of the analyzed cores (Figure 3a). The transition to the siliceous fauna-bearing facies coincides with the FO of *Globigerinoides nepenthes* (Shipboard Scientific Party, 1989; cf. *Globoturborotalita nepenthes*, 11.55 Ma, Wade et al., 2011).

Sediment color ranges from black to white, light grayish greens being the dominant colors. Brighter hues, including occurrence of white (n7/and n8/values), occur below 340 mbsf (~11.0 Ma), above them hues become darker. Color alternations between dark and light hues occur throughout the studied interval (Figure 2); up to 340 mbsf the alternations vary between colors with values of 8 (whites) to 6, from 340 to 320 mbsf (~11.0 to 10.3 Ma) values predominantly range between 7 and 5, whereas above 320 mbsf the range extends from 7 to 4 and includes black layers.

The sedimentary gamma ray component (SGR = K+Th component) and the combined gamma ray (CGR = K+Th+U) logs exhibit matching patterns until ~378 mbsf (~13.3 Ma), at which point both SGR and CGR increase by ~60% and begin to diverge (Figure 2). This is preceded by a decrease of SGR and CGR to below 40 gAPI at 400 mbsf. SGR remains relatively stable, while CGR continually increases within the examined interval. This increase expresses an increase in the U content from less than 1 ppm below 380 mbsf to a continued increase to over 3 ppm near the top of the examined interval. The bulk of this increase, most clearly visible from the U/Th ratio, initiates at ~345 mbsf (~11.2 Ma) with the first appearance of the diatom-bearing nannofossil chalk facies.

4.3. Trace Element Patterns

The main results of the XRF analysis are presented in Figure 4; of note are changes in Si, Mn, and Ba relative to Al and Ca content. Si abundance remains low between ~15 and 11 Ma at which point its abundance increases with respect to Ca (most abundant element in the matrix) and with respect to Al. While there is no significant increase present in samples attributed to nannofossil chalk facies, the Si/Al (Figure 4a) and Si/Ca (Figure 4b) significantly increase in all other facies after 11 Ma with values peaking ~10 Ma, before decreasing toward the end of the studied interval at ~8.8 Ma. The Ti/Fe shows a first increase in maximum values and variability between 14.5 and 14.2 Ma before declining again to lower and more stable values after 13.5 Ma. After 12.5 Ma Ti/Fe values increase again to overall higher and highly variable values that continue until the end of the studied interval ~8.8 Ma.

The ratios of Mn/Ca and Mn/Al decrease from $16.5 \cdot 10^{-3}$ and 5.5 (respectively) around 15 Ma to $4.1 \cdot 10^{-3}$ and 2.0 (respectively) by 14 Ma (Figures 4d and 4e), immediately before the first rise in Ti/Fe values (Figure 4c). After ~12 Ma Mn/Ca and Mn/Al remain low ($6.1 \pm 5.5 \cdot 10^{-3}$ and 1.8 ± 0.7, respectively, $n = 49$) with lowest values coinciding with maxima in Ti/Fe values. Mn/Ca values show significant enrichment in samples taken from diatom-bearing facies ($3.7 \pm 1.7 \cdot 10^{-3}$ in calcareous vs. $10.2 \pm 7.3 \cdot 10^{-3}$ siliceous rich; $n = 27$ and $n = 18$, respectively), which we attribute to biologically controlled changes in the Mn/Ca admixture in calcareous (red sample markers) versus siliceous-rich (gray sample markers) material (compare to Figures 4a and 4b). To show the Mn/Ca ratio in relatively stable admixtures, we show a trend line (red line in Figure 4d) that only considers calcareous samples. For consistency and to aid comparability, this was also done for the Mn/Al record (Figure 4e; see Figures 4a and 4b for comparison with silica abundance).

Ba/Al remains low between 15 and 11.2 Ma where it increases significantly toward a maximum between 10.4 and 10.0 Ma. This increase is consistent across facies, although more substantial in the less calcareous facies. After 10 Ma Ba/Al decreases again but remains overall higher than its initial values before 11 Ma.

4.4. Diatom Abundances

Quantitative counts of diatom concentrations (given as $N*10^9$/g; cf. Bordiga et al., 2015) show a first appearance (more than one specimen per slide) of diatom frustules ~12 Ma (Figure 5a), in accordance with the first occurrence of diatoms and radiolarians by Nigrini et al. (1991), at the base of core 38X. Quantitative analysis shows that while initially diatom abundance is relatively low ($>1 * 10^9$ to max. $1.5 * 10^9$ frustules per gram) abundances rise ~11 Ma reaching maximum abundances of 6–8 $* 10^9$ frustules per gram in diatomaceous samples between 10 and 9.5 Ma. After 9.5 Ma frustule abundances decline again to 1 and $2 * 10^9$/g. Calcareous samples (red sample markers in Figure 5) generally show relatively low frustule counts ($<2 * 10^9$/g). Detected diatom abundances covary closely with the Si/Ca and Si/Al ratios, supporting these ratios as indicators for biogenic silica accumulation at Site 722B (Figures 4a and 4b).

4.5. Carbon and Nitrogen Analyses

4.5.1. TOC and C/N Ratio

Bulk TOC concentrations range between 0.01 and 2.42 wt.%. They fall below 0.3% before 11.5 Ma at which point TOC increases, notably in the diatomaceous marly nannofossil chalk facies, although the increase in TOC occurs across all facies. TOC remains elevated in the examined interval with maximum values (>2 wt.%) between 10.5 and 9.5 Ma (Figure 5b).

The C/N ratio (Figure 5c) ranges between 6.2 and 14.4 and shows a noticeable increase in variability after ~11.4–11.2 Ma resulting in an increase of the average C/N ratio from 7.5 (15–11.4 Ma) to 10.6 (11.2–8.7 Ma). This increase in both variability and average C/N values corresponds to a marked increase in the abundance of biogenic silica at Site 722B (Figure 5a). While C/N ratios are overall higher after 11.4 Ma highest C/N ratios are consistently higher in the diatomaceous marly nannofossil chalk facies than in the nannofossil chalk. This increase in C/N ratio also correlates with a marked increase in the Ba/Al ratio, as well as decreases in the Mn/Al and Mn/Ca ratios in the calcareous nannofossil chalk. After ~9.8 Ma average C/N ratios stay consistently high despite a drop in biogenic silica (Figure 5).

4.5.2. Carbon and Nitrogen Isotopes

$\delta^{15}N$ ranges between 2.4‰ and 6.8‰ with a marked increase around 11.5 Ma with average values rising from 4.3‰ before 11.4 Ma to 5.9‰ after 11.2 Ma (Figure 5d). This increase correlates to the increase in biogenic silica as well as the increase in Ba/Al ratio (Figure 4f), with highest values occurring in the diatomaceous marly nannofossil chalks between 11 and 9.6 Ma.

The $\delta^{13}C_{org}$ ranges between −25.1‰ and −20.3‰. Values of $\delta^{13}C_{org}$ increase throughout the studied interval although it displays internal variability. The increase in $\delta^{13}C_{org}$ at Site 722B (Figure 5e) is inversely correlated to decreasing benthic foraminifer-derived $\delta^{13}C_{carbonate}$ at adjacent Site 731 (Figure 5f). Overall $\delta^{13}C_{org}$ values increase between 15 and 11.5 Ma before reaching relatively stable values (−23‰ to −22‰) between 11.5 and 9.5 Ma. More stable $\delta^{13}C_{org}$ values are also mirrored in relatively stable benthic $\delta^{13}C_{\textit{Cibicidoides}}$ at Site 731 and correspond to the increased values in the Ba/Al ratio (Figure 4f) as well as increasing TOC concentrations (Figure 5b) and the increase in $\delta^{15}N$. Around 9.5 Ma $\delta^{13}C_{org}$ further increases intermittently before reaching values >−21‰ after 9 Ma.

5. Discussion

5.1. The Climatic and Oceanographic Implications of the Langhian-Tortonian Record at Owen Ridge

5.1.1. Facies Patterns and Smear Slide Data

Site 722B records a significant change in the mode of sedimentation during the middle Miocene. The new age model presented here refines the timing of the sedimentation rate decrease (Shipboard Science Party, 1989; Table 1) between 13 and 12 Ma, coinciding with a notable local temperature decrease (Zhuang et al., 2017; Figure 5g). These shifts occur together with a facies change from predominantly calcareous chalks to alternations of chalk and biogenic silica-enriched sediment (termed “marly calcareous nannofossil chalk” during shipboard description), as well as with the initial increase in U observed in the wire logs (Figure 2). After 11.8 Ma (Figure 2) sedimentation rate increases again together with an increase in TOC accumulation (Figure 5b), suggesting a new equilibrium of the system, followed by the occurrence of biogenic silica-rich sediment (diatom-bearing nannofossil chalk; Figure 2) after 12 Ma (black arrowhead in Figures 4e and 5a) and finally to diatomaceous marly nannofossil chalk (Figure 2) and high diatom abundances (Figure 5a) after 10.8 Ma. We also note that this shift roughly coincides with the decrease in downslope transport to the Owen Ridge (Rodriguez et al., 2014) and is thus linked to pelagic productivity changes rather than any changes in the sediment supply at Site 722B. At ~9.3 Ma the diatomaceous marly nannofossil chalk is replaced by diatom-bearing nannofossil chalk with a decrease in sedimentation rate (Figure 2), which may be related to a change in dominant primary producers (Figure 5a) or alternatively the uplift of Owen Ridge (Rodriguez et al., 2014).

The increased preservation of diatoms from 12 Ma onward suggests that silica excess (e.g., Nelson et al., 1995) was gradually established at Site 722B between 13 and 12 Ma. Excluding areas with silica excess, only a fraction of biogenic silica reaches the sediment, and when it does its abundance is often coupled with that of organic carbon (Figures 5a and 5b; Cortese et al., 2004). It is thus likely that changes in oceanic conditions

that favor good preservation of diatom frustules within the sediment may have also contributed to high diatom abundances between 11 and 9.5 Ma. Diatoms and coccoliths generally dominate phytoplankton-derived sediment accumulation under different environmental conditions, with diatoms generally surpassing coccolithophores as the dominant primary producers in the center of upwelling cells (Giraudeau, 1992; Giraudeau et al., 1993). For subsequent interpretations we assume that both mechanisms contributed to the observed increase in biogenic silica accumulation.

While the calcareous nannofossil chalk facies persists throughout the examined interval, it becomes slightly darker in color after diatom occurrences are detected within these facies (Figures 3a and 5b). This would imply that despite the environmental changes occurring in the region during the middle to late Miocene (Gupta et al., 2015; Kroon et al., 1991; Zhuang et al., 2017), the Arabian Sea intermittently reverts to more oligotrophic calcareous nannoplankton-dominated conditions. These facies shifts may thus be reflective of forced changes in productivity (see section 4.1.3 for details), similar to the observed glacial/interglacial variability in the Pleistocene (Clemens & Prell, 2003; Murray & Prell, 1992) with nannofossil chalks occurring predominantly during interglacials.

5.1.2. Sedimentary Dust Proxies and Miocene Wind Patterns in the Arabian Sea

Magnetic susceptibility (MS; Shipboard Scientific Party, 1989), previously established as a dust proxy in this site (de Menocal et al., 1991), decreases from 400 mbsf (14.5 Ma) and drops to a minimum value at ~350 m (11.4 Ma). Low MS levels with a few outliers persist at least until 270 mbsf (top of the examined interval). In parallel, the contribution of detrital components (K+Th) to the total gamma ray counts (Figure 2) diminishes significantly at 400 mbsf (~14.5 Ma) and again at 357 mbsf (~11.8 Ma). While total detrital component is diminished, total dust supply (U/Th) increases (Figure 2) pointing to a significant increase in erosion and wind transport at the sources of Aeolian component to the region (Horn of Africa, the Arabian Peninsula, and the Iranian-Pakistani margin) around 14 Ma. Two subsequent pulses at 12 Ma are matched by dilution of the detrital component with biogenic sediments (calcareous and siliceous). This is in line with our XRF-derived Ti/Fe ratio, which shows increased but highly variable values after ~12 Ma (Figure 4c).

5.1.3. Mn Flux and OMZ Expansion

Manganese abundance in the sediment has an important role in tracing the past extent of the OMZ in the Indian Ocean. Earlier works by Dickens and Owen (1994, 1999) have demonstrated a significant decrease in the supply of Mn to the sediment due to the formation of the OMZ. This is attributed to "Mn redirection" where Mn^{4+} gets reduced to mobile Mn^{2+}, remains in the water column, and gets advected out of the OMZ, decreasing Mn supply to the underlying sediment; Betzler et al. (2016) used the Mn/Ca ratio to identify the expansion of the OMZ to the Maldives at ~13 Ma. At Site 722 the Mn/Ca proxy is less effective (Figure 4e), because of the occurrence of biogenic silica-rich facies, which we alleviate by also examining the Mn/Al ratio (Figure 4f). Furthermore, by considering only data from calcareous nannofossil chalk (Figures 2, 4e, and 4f), a clear decreasing trend in Mn abundance can be observed between 15 and 14 Ma. After that Mn abundance remains low with a possible slight further decrease ~11 Ma. This would suggest that the stable Mn redirection was established as early as ~14.4 Ma and may have slightly intensified around 11 Ma.

5.1.4. Miocene Paleoproductivity at Site 722

Using both Ba/Al and TOC concentrations, two periods of significantly higher productivity can be delineated in Hole 722B, a weaker one between 13.2 and 12.0 Ma and a more significant one from 11.2 to ~9 Ma (Figures 4 and 5). The Ba/Al ratio represents the access of barium relative to the terrigenous component and is commonly interpreted as a paleoproductivity tracer (Bishop, 1988; De Lange et al., 2008; Dymond et al., 1992; Goldberg & Arrhenius, 1958; Rohling et al., 2015; Schmitz et al., 1997; Tachikawa et al., 2015). Productivity increases are often associated with increased organic matter accumulation and oxygen depletion, as demonstrated in the recent past in the Arabian Sea upwelling region (Shimmield, 1992).

The observed C/N ratio and $\delta^{13}C_{org}$ values in the Langhian (Figures 5c and 5e) are consistent with an organic flux of predominantly particulate organic carbon (Deins, 1980; Raymond & Bauer, 2001; Tyson, 1995). The continued increase in the C/N ratio, notably around 11 Ma, paired with the $\delta^{13}C_{org}$ of $-21.9 \pm 1.0‰$ suggests either an increase in local primary productivity and organic matter drawdown in the sediment or higher influx of terrestrial C3 plant-derived carbon (Hansell & Carlson, 2015). As BIT index results from GDGT analysis by Zhuang et al. (2017) indicate a very small terrestrial organic component, paired with the increase in TOC (Gupta et al., 2015; Figure 5b), the observed changes in C/N and $\delta^{13}C_{org}$ suggest an increase

in primary productivity around 11.5 Ma. As organic matter sinks through the water column, it is remineralized, releasing isotopically light dissolved inorganic carbon (DIC, Hansell & Carlson, 2015). The increase in $\delta^{13}C_{org}$ (derived from the upper water column) paired with a matching decrease in $\delta^{13}C_{Cibicides\ spp.}$ (Gupta et al., 2015; Figures 5e and 5f), which records the deep water DIC, points to a significant partition of carbon to organic matter at the surface and transfer of an increasingly larger fraction of the carbon to DIC in the deep water. The $\delta^{13}C_{Cibicides\ spp.}$ shift at Site 722 is comparable in magnitude (1‰ lower relative to early Miocene values) to the observed decoupling in benthic foraminifera $\delta^{13}C$ values between the Pacific and the Atlantic Oceans (Cramer et al., 2009). However, the drop in Site 722 occurs around 12 Ma, ~3 Myr before the shift in the Pacific. This difference indicates that this shift is a local northern Indian Ocean effect, rather than related to the maturation of deep water in the late Miocene.

Presently, denitrification is the dominant mechanism of nitrogen loss in the Arabian Sea during reduced oxygen concentrations in the water column (Ward et al., 2009). As a significant portion of nitrogen partitions within the OMZ, it results in a significant shift to positive $\delta^{15}N$ values in the organic matter deposited in the sediment. The increase in $\delta^{15}N$ (Figure 5d) in conjunction with increased abundance of diatoms, TOC, and the Ba/Al ratio suggests that denitrification is occurring in the water body in response to increased organic matter load (Narkis et al., 1979). Based on previous studies in the region (Altabet et al., 1995; Altabet et al., 1999; Gaye-Haake et al., 2005; Tripathi et al., 2017) $\delta^{15}N$ values above 6‰ have been ascribed to indicate sustained denitrification in the water column. In the Miocene record of Site 722, $\delta^{15}N$ increases above 6‰ for the first time ~11 Ma. $\delta^{15}N$ values remain elevated until 9.6 Ma suggesting the occurrence of at least intermittent denitrification ($\delta^{15}N > 6‰$) over this time interval. Values decrease at ~9.6 Ma before increasing again ~8.8 Ma. We interpret this decrease in $\delta^{15}N$ values as weakening denitrification due to a reduction in primary productivity after the end of the diatomaceous interval. Interestingly, the principle phase of denitrification in the eastern Arabian Sea (Site U1456, Tripathi et al., 2017) was reported to initiate at 3 Ma. However, the published data from Site U1456 do include $\delta^{15}N \geq 6‰$ values prior to the 8.2–9.2 Ma hiatus, suggesting that denitrification was also recorded in the eastern Arabian Sea at that time.

5.2. Contextualizing Miocene Upwelling in the Arabian Sea

5.2.1. Tectonic Preconditioning of the Modern Indian Ocean Circulation

The Indian Ocean has gone through a major reorganization during the Burdigalian with the restriction of the Indonesian Gateway to the Pacific Ocean (Hall, 2009; Kuhnt et al., 2004) and complete closure of the Tethyan Seaway (= Mesopotamian Gateway) to the Mediterranean (Bialik et al., 2019; Harzhauser et al., 2007; Reuter et al., 2009; Reuter et al., 2013; Rögl, 1998). Consequently, at least since ~14 Ma (with the final closure of the Tethyan Seaway in the Mesopotamian Trough), the Indian Ocean's only major deepwater connection was located in the Southern Ocean. Marine faunal exchange (Harzhauser et al., 2009; Harzhauser & Fehse, 2007) between the Mediterranean and Indo-Pacific realm ceased even before (~22–20 Ma) suggesting a significant biogeographic separation in the Aquitanian. This may have also severely restricted deepwater exchange through the Tethyan Seaway by that time. Incidentally, ~22 Ma also marked the inception of wind-blown deposits on the western Chinese Loess Plateau and increase in MS in the Maldives, both interpreted as the onset of monsoon activity (Betzler et al., 2016; Guo et al., 2002), lending credence to the hypothesis that the closure of the Tethyan Seaway was a significant step in the evolution of SAM (Fluteau et al., 1999; Hamon et al., 2013; Zhongshi et al., 2007). Synthesizing these previous studies with our new data consequently suggests that the restriction of both its tropical connections ~14 Ma provided the topography necessary to form a new closed circulation mode in the northern Indian Ocean (Gourlan et al., 2008; Hamon et al., 2013; Le Houedec et al., 2012).

5.2.2. Forcing and Feedbacks of Middle to late Miocene Monsoonal Upwelling

With the initiation of global cooling in the early Langhian (~15 Ma; Flower & Kennett, 1994) and dropping atmospheric pCO_2 (Pagani et al., 1999) Antarctica began to glaciate, generating cold, salty deep, and intermediate waters (Hamon et al., 2013). This in turn also initiated a northward migration of the Southern Hemisphere westerlies culminating in a reorganization of the southern hemisphere Hadley cells by ~12 Ma (Groeneveld et al., 2017; Figure 6).

As upwelling along the Oman margin is directly linked to Indian Ocean hydroclimate and thus Indian summer monsoon intensity (Currie et al., 1973; Fischer et al., 2002; Manghnani et al., 1998; Murtugudde et al.,

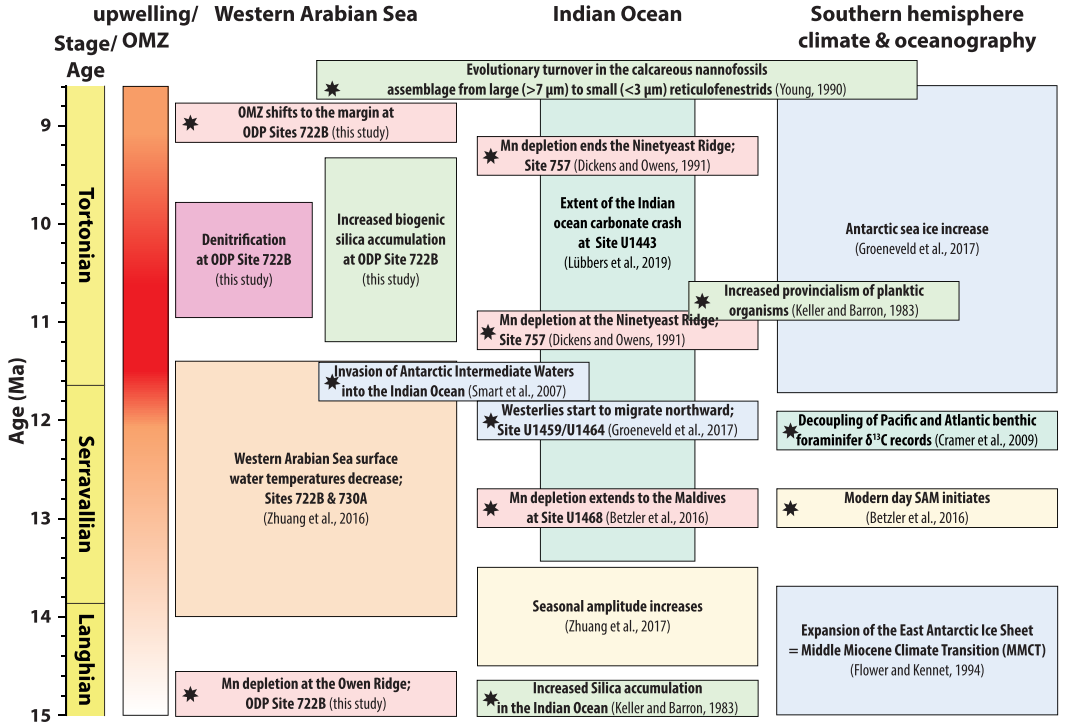

Figure 6. Principle events in the Western Arabian Sea, Indian Ocean, and southern hemisphere related to the evolution of Arabian Sea upwelling and northwestern Indian Ocean OMZ intensity (red shaded area; darker shades reflect stronger upwelling). Arabian Sea SST data and seasonality inference from Zhuang et al. (2017); Foraminifera data from Keller and Baron (1983), Kroon et al. (1991), and Gupta et al. (2015); Oceanic isotopes data from Cramer et al. (2009); Antarctic Ice Sheet from Flower and Kennett (1994); Australian Climate from Groeneveld et al. (2017); SAM and Maldives state from Betzler et al. (2016, 2018); southern Indian Ocean Intermediate water state from Smart et al. (2007). Indian Ocean carbonate crash after Lübbers et al. (2019).

2007), it is crucial to consider the initiation of upwelling in the Arabian Sea, between 15 and 14 Ma in a climatic context. Both the initial drop in sea surface temperature and increased seasonal amplitude (Zhuang et al., 2017), as well as the initiation of Mn depletion (Figures 4d and 4e), can be directly linked to the intensification of the prevailing wind system controlling the SAM and thus Oman Margin upwelling (Betzler et al., 2016). At the same time upwelled water likely began to progressively incorporate more Antarctic Intermediate Waters that today are a major component of the waters upwelling in the Arabian Sea (e.g., Munz et al., 2017). These changes likely led to an increase in nutrient availability across much of the Indian Ocean as evidenced by the initiation of significant biogenic silica accumulation (Keller & Barron, 1983; Figure 6).

Between 13 and 12 Ma the increasing southern hemisphere thermal gradient had begun to push both the subtropical high and the ITCZ further north (Groeneveld et al., 2017; Figure 6). The associated intensification of the Mascarene high pressure cell would then have strengthened the Somali/Findlater Jets and thus SAM winds as a direct consequence (Figure 1; Cao et al., 2017; Pound et al., 2012; Wu, 2017). This coupled atmosphere-ocean reorganization resulted in a significant shift of wind and current patterns in the northern Indian Ocean as well as the initiation of the modern SAM mode at ~13 Ma (Betzler et al., 2016; Gupta et al., 2015). As a result, nutrient upwelling increased in the western Arabian Sea and the OMZ expanded, as far south as the Maldives. This expansion had a significant effect on planktonic foraminiferal populations (see below), heralding a noticeable increase in the abundance of *Globigerina bulloides* in the western Indian Ocean (Gupta et al., 2015; Huang et al., 2007; Kroon et al., 1991). Decreasing oxygen levels during OMZ expansion may also be linked to the extinction of several benthic foraminifera at that time in the Indo-Pacific (Keller & Barron, 1983).

Toward the end of the Serravallian (~12 Ma), a significant low-amplitude node in orbital eccentricity (Laskar et al., 2011) intensified sea ice accumulation (Verducci et al., 2009). These cooler conditions increased the

vigor of deepwater circulation and the extent of Antarctic bottom and intermediate waters into the western Indian Ocean and Arabian Sea (Smart et al., 2007; Figure 6). The resulting current reorganization was the product of cooling of the deep waters and rearrangement of oceanic gateways (namely, the Panama Isthmus and Iceland sill), leading to a decoupling of the Atlantic and Pacific basins (Cramer et al., 2009). In the Indian Ocean this decoupling manifested in increased provincialism of several planktonic foraminifera groups (Keller & Barron, 1983; Figure 6). The expansion of young and cool Antarctic deep and intermediate water into the Indian ocean led to cooler waters upwelling in the western Arabian Sea (Zhuang et al., 2017). These nutrient enriched waters (Ba/Al increase) promoted significant accumulation of biogenic silica (Figures 4 and 5). Moreover, the increased organic load led to the establishment of water body denitrification (observed in this study by the $\delta^{15}N$ trend; Figure 5d) ~11.5 Ma in the western Arabian Sea (Figure 6). The observed increase in biogenic silica (i.e., diatom accumulation) at Site 722B closely correlates with biogenic silica and benthic foraminifer-derived productivity records from Site 714 (Boersma & Mikkelsen, 1990) and increased productivity and carbon export flux at Site U1443 (Lübbers et al., 2019), showing that this productivity signal is present throughout the northern Indian Ocean. At this time, there is also evidence that the OMZ expanded further southward, reaching the Ninety East Ridge (Site 757, Dickens & Owen, 1999; Figure 6). Finally, we also note that this reduction in biogenic silica is followed by a dominance in small r-selected (=high nutrient adapted) Reticulofenestra at Site 722B. This dominance of small reticulofenestrids, and thus carbonate producers, in the planktonic assemblage coincides with a major evolutionary turnover in these nannofossil taxa (Young, 1990; Figure 6).

During the mid-Tortonian, the extent of the northern Indian Ocean OMZ appears to have reduced again (Dickens & Owen, 1994, 1999). In the Arabian Sea, this is recognized by a notable shift of *Globigerina bulloides* from the Owen Ridge to the continental margin (Gupta et al., 2015) and a reduction in the accumulation of biogenic silica at Site 722B (~9.5 Ma; Figure 5a). These changes may be linked to a temporary decrease in monsoonal wind intensity (cf. Figure 1), that would weaken the upwelling in the Arabian Sea (Site 722B). Furthermore, latitudinal thermal gradient would have been reduced by an increase in solar irradiation in the high latitudes (Laskar et al., 2011). The coupling of monsoon driven upwelling and insolation is well documented in both proxy studies of the Holocene and Pleistocene (Clemens et al., 1991; Emeis et al., 1995; Munz et al., 2017; Prell & Van Campo, 1986) as well as modelling studies (Murtugudde et al., 2007) on decadal to Milankovitch time scales. The phenomenon of reduced hemispheric thermal gradients during this time is supported by a contemporary decrease in rainfall over the European continent (Böhme et al., 2008) and global vegetation dynamics (Pound et al., 2012). Modeling studies (e.g., Zhang et al., 2014) further indicate that insolation changes had a much more pronounced impact on ITCZ shifts in the region after the closure of the Tethyan Seaway. Alternatively, the establishment of deepwater passages in the Indonesian Archipelago after 10 Ma (Hall, 2009; Kuhnt et al., 2004) may have contributed to this shift by reopening the tropical deepwater connection to the Pacific Ocean at that time. In summary, one or even a combination of these events could have contributed to the weakening of the Arabian Sea upwelling that then resulted in a less extensive OMZ.

5.2.3. A Link to the Indian Ocean Carbonate Crash?

Interestingly, the increase in biogenic silica burial at Site 722B occurs at the same time as the carbonate crash observed at the Ninety East ridge in the Indian Ocean (Lübbers et al., 2019). At this time reduced carbonate accumulation is also recorded in the Pacific and the Caribbean (e.g., Jiang et al., 2007). Our data thus offer additional evidence that this late Miocene reduction in carbonate accumulation rate occurred in all three major ocean basins. Crucially, however, diatom abundances at Site 722B indicate that significant changes in surface waters primary producers (a shift to predominantly siliceous phytoplankton) could also have been an additional contributing factor to decreasing global carbonate accumulation, without the need for a reduction in overall surface productivity (i.e., Diester-Haas et al., 2004). Furthermore, the continued presence of moderately to even well-preserved nannofossils between 12 and 9 Ma shows that corrosive waters were limited to the deeper ocean (> ~2,000 m) in the Arabian Sea, which indicates that carbonate dissolution was not the cause for the "carbonate crash" at our study site.

Overall, this suggests that the expansion of cold, nutrient-rich, Antarctic deep and intermediate waters may have had a major impact on primary productivity and plankton communities along the Oman Margin, while also affecting carbonate preservation in the deeper parts of the Indian Ocean (e.g.: Lübbers et al., 2019). The effects of this shift in upwelling conditions are also recognized in contemporary records from other major upwelling regions such as the Benguela Upwelling system (Rommerskirchen et al., 2011).

We hypothesize that Antarctic sea ice expansion (Flower & Kennet, 1994), together with a strengthening of the Antarctic Circumpolar Current and northward shift in the southern hemisphere Hadley cells (Groeneveld et al., 2017), led to a long-term increase in the strength of the Somali/Findlater Jets and thus summer monsoon winds during the Miocene (Betzler et al., 2016; Gadgil, 2018). This resulted in the stepwise establishment of a more modern-like global coupled ocean-atmospheric circulation as a result of increasing latitudinal thermal gradients during the middle Miocene Climate Transition. The increased advection of cool nutrient-rich waters caused by these events, in turn, had a profound impact on upwelling along the Oman Margin during the middle and late Miocene (Figure 6). Consequently, the increased upwelling of cold nutrient-rich waters may have heralded a change in dominant primary producers, leading to the global proliferation of widespread diatom blooms (Keller & Barron, 1983; Koizumi & Yamamoto, 2018; Figure 6). Antarctic deep waters also became more corrosive during this time and may have played a key role in the Miocene carbonate crash (e.g., Jiang et al., 2007; Lübbers et al., 2019).

6. Conclusions

The Miocene establishment of the western Indian Ocean upwelling and OMZ was a gradual process that occurred over a period of up to 5 Myr. With the establishment of favorable tectonic configuration, the initial formation likely occurred between 14.8 and 14.0 Ma as a direct response to the glaciation of Antarctica, shown by a decreasing Mn concentration. It further intensified around 13 Ma, resulting in upwelling-derived nutrient excess (Ba/Al) that resulted in increased biogenic silica accumulation in the western Indian Ocean. This intensification lead to the expansion of the OMZ at least as far as the Maldives. Further intensification between 11.5 and 11.0 Ma leads to a late Miocene apex in upwelling which lasted until 9.6 Ma. This productivity maximum is marked by denitrification and can be linked to a significant expansion of the OMZ possibly south of the equator and as far as east as the Ninety East Ridge (Figure 6). After 9.6 Ma the OMZ appears to have retracted and shifted closer to the Oman margin. Our data furthermore shed new light in the evolution of primary productivity, denitrification, and organic matter accumulation at Site 722B during the middle-late Miocene and shows a close link with the documented evolution of global ocean-atmospheric circulation system during that time. Our productivity data also provide a clear link between upwelling in the Arabian Sea to the "biogenic bloom" in the wider Indian Ocean. These results emphasize the direct link of Antarctic deepwater expansion, and related worldwide establishment of cold high productivity upwelling zones, to the expansion of the Indian Ocean OMZ. Finally, the enhanced circulation of corrosive Antarctic deep waters also played a role in the occurrence of the deep marine carbonate crash in the middle-late Miocene.

Acknowledgments
O. M. B. and G. A. contributed equally and share first authorship. This research used samples and data provided by the International Ocean Discovery Program (IODP). This study was partially funded by GIF project MioEast (Grants 1-1336-301.8/2016) awarded to N. D. W. (in collaboration with Christian Betzler and Martin Frank) and contributes to JSPS Grant 17H07412 awarded to G. A. The authors would like to thank IODP and especially Dr. Lallan Gupta and the Kochi Core Repository (KCC) for access to and diligent sampling of ODP Site 722B. N. Taha, Y. Yoshikawa, and Y. Niyazi are thanked for technical and analytical assistance and Y. Lahan for input regarding oceanic circulation and chlorophyll patterns. We are grateful for the input of 2 anonymous reviewers that help to improve this manuscript. Ellen Thomas and Margret Steinthorsdottir are thanked for their editorial expertise and handling of this manuscript. The data generated for Site 722 presented in this study are available on PANGAEA, doi: 10.1594/PANGAEA.910897 (Diatom and nannofossil counts); 10.1594/PANGAEA.910900 (XRF data); 10.1594/PANGAEA.910901 (OM stable isotopes); and 10.1594/PANGAEA.910902 (Age model).

References

Altabet, M. A., Francois, R., Murray, D. W., & Prell, W. L. (1995). Climate-related variations in denitrification in the Arabian Sea from sediment $^{15}N/^{14}N$ ratios. *Nature*, *373*(6514), 506–509. https://doi.org/10.1038/373506a0

Altabet, M. A., Murray, D. W., & Prell, W. L. (1999). Climatically linked oscillations in Arabian Sea denitrification over the past 1 m.y.: Implications for the marine N cycle. *Paleoceanography*, *14*(6), 732–743. https://doi.org/10.1029/1999PA900035

Backman, J., Raffi, I., Rio, D., Fornaciari, E., & Pälike, H. (2012). Biozonation and biochronology of Miocene through Pleistocene calcareous nannofossils from low and middle latitudes. *Newsletters on Stratigraphy*, *45*(3), 221–244.

Banse, K., Naqvi, S. W. A., Narvekar, P. V., Postel, J. R., & Jayakumar, D. A. (2014). Oxygen minimum zone of the open Arabian Sea: Variability of oxygen and nitrite from daily to decadal timescales. *Biogeosciences*, *11*(8), 2237–2261. https://doi.org/10.5194/bg-11-2237-2014

Betzler, C., Eberli, G. P., Kroon, D., Wright, J. D., Swart, P. K., Nath, B. N., et al. (2016). The abrupt onset of the modern South Asian Monsoon winds. *Scientific Reports*, *6*(1), 29838. https://doi.org/10.1038/srep29838

Bialik, O. M., Frank, M., Betzler, C., Zammit, R., & Waldmann, N. D. (2019). Two-step closure of the Miocene Indian Ocean gateway to the Mediterranean. *Scientific Reports*, *9*(1), 8842. https://doi.org/10.1038/s41598-019-45308-7

Bishop, J. K. B. (1988). The barite-opal-organic carbon association in oceanic particulate matter. *Nature*, *332*(6162), 341–343. https://doi.org/10.1038/332341a0

Boersma, A., & Mikkelsen, N. (1990). Miocene-age primary productivity episodes and oxygen minima in the central equatorial Indian Ocean. In R. A. Duncan, J. Backman, & L. C. Peterson (Eds.), *Proceedings of the Ocean Drilling Program, 115 Scientific Results* (pp. 589–609). College Station, TX: Ocean Drilling Program. https://doi.org/10.2973/odp.proc.sr.115.162.1991

Böhme, M., Ilg, A., & Winklhofer, M. (2008). Late Miocene "washhouse" climate in Europe. *Earth and Planetary Science Letters*, *275*(3–4), 393–401. https://doi.org/10.1016/j.epsl.2008.09.011

Bordiga, M., Bartol, M., & Henderiks, J. (2015). Absolute nannofossil abundance estimates: Quantifying the pros and cons of different techniques. *Revue de Micropaléontologie*, *58*(3), 155–165. https://doi.org/10.1016/j.revmic.2015.05.002

Cao, W., Zahirovic, S., Flament, N., Williams, S., Golonka, J., & Müller, R. D. (2017). Improving global paleogeography since the late Paleozoic using paleobiology. *Biogeosciences*, *14*(23), 5425–5439. https://doi.org/10.5194/bg-14-5425-2017

Clemens, S. C., Prell, W., Murray, D., Shimmield, G., & Weedon, G. (1991). Forcing mechanisms of the Indian Ocean monsoon. *Nature*, *353*(6346), 720–725. https://doi.org/10.1038/353720a0

Clemens, S. C., & Prell, W. L. (2003). A 350,000 year summer-monsoon multi-proxy stack from the Owen Ridge, Northern Arabian Sea. *Marine Geology*, *201*(1–3), 35–51. https://doi.org/10.1016/S0025-3227(03)00207-X

Clift, P. D., & Webb, A. A. G. (2018). A history of the Asian monsoon and its interactions with solid Earth tectonics in Cenozoic South Asia. In P. J. Treloar, & M. P. Searle (Eds.), *Himalayan Tectonics: A Modern Synthesis* (pp. 631–652). London, Special Publications 483: Geological Society. https://doi.org/10.1144/SP483.1

Cortese, G., Gersonde, R., Hillenbrand, C. D., & Kuhn, G. (2004). Opal sedimentation shifts in the World Ocean over the last 15 Myr. *Earth and Planetary Science Letters*, *224*(3–4), 509–527. https://doi.org/10.1016/j.epsl.2004.05.035

Cramer, B. S., Toggweiler, J. R., Wright, J. D., Katz, M. E., & Miller, K. G. (2009). Ocean overturning since the late cretaceous: Inferences from a new benthic foraminiferal isotope compilation. *Paleoceanography*, *24*(4), 1–14. https://doi.org/10.1029/2008PA001683

Currie, R. I., Fisher, A. E., & Hargreaves, P. M. (1973). Arabian sea upwelling. In B. Zeitzschel, & S. A. Gerlach (Eds.), *The Biology of the Indian Ocean* (pp. 37–52). Berlin, Heidelberg: Springer Berlin Heidelberg. https://doi.org/10.1007/978-3-642-65468-8_4

De Lange, G. J., Thomson, J., Reitz, A., Slomp, C. P., Speranza Principato, M., Erba, E., & Corselli, C. (2008). Synchronous basin-wide formation and redox-controlled preservation of a Mediterranean sapropel. *Nature Geoscience*, *1*(9), 606–610. https://doi.org/10.1038/ngeo283

de Menocal, P., Bloemendal, J., & King, J. (1991). A rock-magnetic record of monsoonal dust deposition to the Arabian Sea: Evidence for a shift in the mode of deposition at 2.4 Ma. In *Proceedings of the Ocean Drilling Program, 117 Scientific Results* (pp. 389–407). College Station, TX: Ocean Drilling Program. https://doi.org/10.2973/odp.proc.sr.117.178.1991

Deins, P. (1980). The isotopic composition of reduced organic carbon. In P. Fritz, & J. C. Fontes (Eds.), *The Terrestrial Environment, A - A volume in Handbook of Environmental Isotope Geochemistry* (pp. 329–406). Amsterdam: Elsevier. https://doi.org/10.1016/B978-0-444-41780-0.50015-8

Dickens, G. R., & Owen, R. M. (1994). Late Miocene-early Pliocene manganese redirection in the central Indian Ocean: Expansion of the intermediate water oxygen minimum zone. *Paleoceanography*, *9*(1), 169–181. https://doi.org/10.1029/93PA02699

Dickens, G. R., & Owen, R. M. (1999). The Latest Miocene-Early Pliocene biogenic bloom: A revised Indian Ocean perspective. *Marine Geology*, *161*(1), 75–91. https://doi.org/10.1016/S0025-3227(99)00057-2

Dymond, J., Suess, E., & Lyle, M. (1992). Barium in deep-sea sediment: A geochemical proxy for paleoproductivity. *Paleoceanography*, *7*(2), 163–181. https://doi.org/10.1029/92PA00181

Emeis, K.-C., Anderson, D. M., Doose, H., Kroon, D., & Schulz-Bull, D. (1995). Sea-surface temperatures and the history of monsoon upwelling in the northwest Arabian Sea during the last 500,000 years. *Quaternary Research*, *43*(3), 355–361. https://doi.org/10.1006/qres.1995.1041

Findlater, J. (1969). Interhemispheric transport of air in the lower troposphere over the western Indian Ocean. *Quarterly Journal of the Royal Meteorological Society*, *95*(404), 400–403. https://doi.org/10.1002/qj.49709540412

Fischer, A. S., Weller, R. A., Rudnick, D. L., Eriksen, C. C., Lee, C. M., Brink, K. H., ... Leben, R. R. (2002). Mesoscale eddies, coastal upwelling, and the upper-ocean heat budget in the Arabian Sea. *Deep Sea Research Part II: Topical Studies in Oceanography*, *49*(12), 2231–2264. https://doi.org/10.1016/S0967-0645(02)00036-X

Flower, B. P., & Kennett, J. P. (1994). The middle Miocene climatic transition: East Antarctic ice sheet development, deep ocean circulation and global carbon cycling. *Palaeogeography, Palaeoclimatology, Palaeoecology*, *108*(3–4), 537–555. https://doi.org/10.1016/0031-0182(94)90251-8

Fluteau, F., Ramstein, G., & Besse, J. (1999). Simulating the evolution of the Asian and African monsoons during the past 30 million years using an atmospheric general circulation model. *Journal of Geophysical Research*, *104*, 11995–12018. https://doi.org/10.1029/1999JD900048

Gadgil, S. (2018). The monsoon system: Land–sea breeze or the ITCZ? *Journal of Earth System Science*, *127*(1), 1. https://doi.org/10.1007/s12040-017-0916-x

Garcia, H. E. K., Weathers, C. R., Paver, I., Smolyar, T. P., Boyer, R. A., Locarnini, M. M., et al. (2018). In A. Mishonov (Ed.), *World Ocean Atlas 2018, Volume 3: Dissolved Oxygen, Apparent Oxygen Utilization, and Oxygen Saturation*. NOAA Atlas NESDIS 83.

Gaye-Haake, B., Lahajnar, N., Emeis, K.-C., Unger, D., Rixen, T., Suthhof, A., et al. (2005). Stable nitrogen isotopic ratios of sinking particles and sediments from the northern Indian Ocean. *Marine Chemistry.*, *96*(3-4), 243–255. https://doi.org/10.1016/j.marchem.2005.02.001

Giraudeau, J. (1992). Distribution of recent nannofossils beneath the Benguela system: Southwest African continental margin. *Marine Geology*, *108*(2), 219–237. https://doi.org/10.1016/0025-3227(92)90174-G

Giraudeau, J., Monteiro, P. M. S., & Nikodemus, K. (1993). Distribution and malformation of living coccolithophores in the northern Benguela upwelling system off Namibia. *Marine Micropaleontology*, *22*(1–2), 93–110. https://doi.org/10.1016/0377-8398(93)90005-I

Goldberg, E. D., & Arrhenius, G. O. S. (1958). Chemistry of Pacific pelagic sediments. *Geochimica et Cosmochimica Acta*, *13*(2–3), 153–212. https://doi.org/https://doi.org/10.1016/0016-7037(58)90046-2

Gourlan, A. T., Meynadier, L., & Allègre, C. J. (2008). Tectonically driven changes in the Indian Ocean circulation over the last 25 Ma: Neodymium isotope evidence. *Earth and Planetary Science Letters*, *267*(1–2), 353–364. https://doi.org/10.1016/j.epsl.2007.11.054

Groeneveld, J., Henderiks, J., Renema, W., McHugh, C. M., De Vleeschouwer, D., Christensen, B. A., et al. (2017). Australian shelf sediments reveal shifts in Miocene Southern Hemisphere westerlies. *Science Advances*, *3*(5), e1602567. https://doi.org/10.1126/sciadv.1602567

Guo, Z. T., Ruddiman, W. F., Hao, Q. Z., Wu, H. B., Qiao, Y. S., Zhu, R. X., et al. (2002). Onset of Asian desertification by 22 Myr ago inferred from loess deposits in China. *Nature*, *416*(6877), 159–163. https://doi.org/10.1038/416159a

Gupta, A. K., Yuvaraja, A., Prakasam, M., Clemens, S. C., & Velu, A. (2015). Evolution of the South Asian monsoon wind system since the late Middle Miocene. *Palaeogeography, Palaeoclimatology, Palaeoecology*, *438*, 160–167. https://doi.org/10.1016/j.palaeo.2015.08.006

Hall, R. (2009). Southeast Asia's changing palaeogeography. *Blumea: Journal of Plant Taxonomy and Plant Geography*, *54*(1), 148–161. https://doi.org/10.3767/000651909X475941

Hamon, N., Sepulchre, P., Lefebvre, V., & Ramstein, G. (2013). The role of eastern tethys seaway closure in the middle Miocene climatic transition (ca. 14 Ma). *Climate of the Past*, *9*(6), 2687–2702. https://doi.org/10.5194/cp-9-2687-2013

Hansell, D. A., & Carlson, C. A. (2015). *Biogeochemistry of marine dissolved organic matter*, *Biogeochemistry of marine dissolved organic matter*. Amsterdam, Netherlands: Elsevier. https://doi.org/10.1016/C2012-0-02714-7

Harzhauser, M., & Fehse, D. (2007). Oligocene and Aquitanian gastropod faunas from the Sultanate of Oman and their biogeographic implications for the early western Indo-Pacific. *Palaeontographica Abteilung A*, *280*(4–6), 75–121. https://doi.org/10.1127/pala/280/2007/75

Harzhauser, M., Kroh, A., Mandic, O., Piller, W. E., Göhlich, U., Reuter, M., & Berning, B. (2007). Biogeographic responses to geodynamics: A key study all around the Oligo–Miocene Tethyan Seaway. *Zoologischer Anzeiger—A Journal of Comparative Zoology*, *246*(4), 241–256. https://doi.org/10.1016/j.jcz.2007.05.001

Harzhauser, M., Reuter, M., Piller, W. E., Berning, B., Kroh, A., & Mandic, O. (2009). Oligocene and Early Miocene gastropods from Kutch (NW India) document an early biogeographic switch from Western Tethys to Indo-Pacific. *Palaontologische Zeitschrift*, *83*(3), 333–372. https://doi.org/10.1007/s12542-009-0025-5

Herold, N., Huber, M., & Müller, R. D. (2011). Modeling the Miocene climatic optimum. Part I: Land and atmosphere. *Journal of Climate*, *24*(24), 6353–6372. https://doi.org/10.1175/2011JCLI4035.1

Holbourn, A. E., Kuhnt, W., Clemens, S. C., Kochhann, K. G. D., Jöhnck, J., Lübbers, J., & Andersen, N. (2018). Late Miocene climate cooling and intensification of southeast Asian winter monsoon. *Nature Communications*, *9*(1), 1584. https://doi.org/10.1038/s41467-018-03950-1

Huang, Y., Clemens, S. C., Liu, W., Wang, Y., & Prell, W. L. (2007). Large-scale hydrological change drove the late Miocene C_4 plant expansion in the Himalayan foreland and Arabian Peninsula. *Geology*, *35*(6), 531. https://doi.org/10.1130/G23666A.1

Ivanova, E. (2009). *The global thermohaline paleocirculation*. Dordrecht: Springer Netherlands. https://doi.org/10.1007/978-90-481-2415-2

Jiang, S., Wise, S. W. Jr., & Wang, Y. (2007). Cause of the middle/late Miocene carbonate crash: Dissolution or low productivity? In D. A. H. Teagle, D. S. Wilson, G. D. Acton, & D. A. Vanko (Eds.), *Proceedings of the Ocean Drilling Program, 206 Scientific Results* (pp. 1–24). College Station, TX: Ocean Drilling Program. https://doi.org/10.2973/odp.proc.sr.206.013.2007

Keller, G., & Barron, J. A. (1983). Paleoceanographic implications of Miocene deep-sea hiatuses. *Geological Society of America Bulletin*, *94*(5), 590–613. https://doi.org/10.1130/0016-7606(1983)94<590:PIOMDH>2.0.CO;2

Koizumi, I., & Yamamoto, H. (2018). Diatom ooze and diatomite–diatomaceous sediments in and around the North Pacific Ocean. *JAMSTEC Report of Research and Development*, *27*(0), 26–46. https://doi.org/10.5918/jamstecr.27.26

Kroon, D., Steens, T. N. F., & Troelstra, S. R. R. (1991). Onset of monsoonal related upwelling in the western Arabian sea as revealed by planktonic foraminifers. *Proceedings of the Ocean Drilling Program, Scientific Results*, *117*, 257–263. https://doi.org/10.2973/odp.proc.sr.117.126.1991

Kuhnt, W., Holbourn, A., Hall, R., Zuvela, M., & Käse, R. (2004). Neogene history of the Indonesian throughflow, 299–320. https://doi.org/10.1029/149GM16

Laskar, J., Fienga, A., Gastineau, M., & Manche, H. (2011). La2010: A new orbital solution for the long-term motion. *89*, 1–15.

Le Houedec, S., Meynadier, L., & Allègre, C. J. (2012). Nd isotope systematics on ODP Sites 756 and 762 sediments reveal major volcanic, oceanic and climatic changes in South Indian Ocean over the last 35Ma. *Earth and Planetary Science Letters*, *327-328*, 29–38. https://doi.org/10.1016/j.epsl.2012.01.019

Lewis, B. L., & Luther, G. W. III (2000). Processes controlling the distribution and cycling of manganese in the oxygen minimum zone of the Arabian Sea. *Deep Sea Research Part II: Topical Studies in Oceanography*, *47*(7–8), 1541–1561. https://doi.org/10.1016/S0967-0645(99)00153-8

Lübbers, J., Kuhnt, W., Holbourn, A. E., Bolton, C. T., Gray, E., Usui, Y., et al. (2019). The middle to late Miocene "carbonate crash" in the equatorial Indian Ocean. *Paleoceanography and Paleoclimatology*, 2018PA003482. https://doi.org/10.1029/2018PA003482

Manghnani, V., Morrison, J. M., Hopkins, T. S., & Böhm, E. (1998). Advection of upwelled waters in the form of plumes off Oman during the Southwest Monsoon. *Deep Sea Research Part II: Topical Studies in Oceanography*, *45*(10–11), 2027–2052. https://doi.org/10.1016/S0967-0645(98)00062-9

McCreary, J. P., Yu, Z., Hood, R. R., Vinaychandran, P. N., Furue, R., Ishida, A., & Richards, K. J. (2013). Dynamics of the Indian Ocean oxygen minimum zones. *Progress in Oceanography*, *112-113*, 15–37. https://doi.org/10.1016/j.pocean.2013.03.002

Morrison, J., Codispoti, L., Smith, S. L., Wishner, K., Flagg, C., Gardner, W. D., et al. (1999). The oxygen minimum zone in the Arabian Sea during 1995. *Deep Sea Research Part II: Topical Studies in Oceanography*, *46*(8–9), 1903–1931. https://doi.org/10.1016/S0967-0645(99)00048-X

Munz, P. M., Steinke, S., Böll, A., Lückge, A., Groeneveld, J., Kucera, M., & Schulz, H. (2017). Decadal resolution record of Oman upwelling indicates solar forcing of the Indian summer monsoon (9–6 ka). *Climate of the Past*, *13*(5), 491–509. https://doi.org/10.5194/cp-13-491-2017

Murray, D. W., & Prell, W. L. (1992). Late Pliocene and Pleistocene climatic oscillations and monsoon upwelling recorded in sediments from the Owen Ridge, northwestern Arabian Sea. *Geological Society, London, Special Publications*, *64*(1), 301–321. https://doi.org/10.1144/GSL.SP.1992.064.01.20

Murtugudde, R., Seager, R., & Thoppil, P. (2007). Arabian Sea response to monsoon variations. *Paleoceanography*, *22*(4), n/a–n/a. https://doi.org/10.1029/2007PA001467

Narkis, N., Rebhun, M., & Sheindorf, C. H. (1979). Denitrification at various carbon to nitrogen ratios. *Water Research*, *13*(1), 93–98. https://doi.org/10.1016/0043-1354(79)90259-8

Nelson, D. M., Tréguer, P., Brzezinski, M. A., Leynaert, A., & Quéguiner, B. (1995). Production and dissolution of biogenic silica in the ocean: Revised global estimates, comparison with regional data and relationship to biogenic sedimentation. *Global Biogeochemical Cycles*, *9*(3), 359–372. https://doi.org/10.1029/95GB01070

Ogawa, N. O., Nagata, T., Kitazato, H., & Ohkouchi, N. (2010). Ultra sensitive elemental analyzer/isotope ratio mass spectrometer for stable nitrogen and carbon isotope analyses. In N. Ohkouchi, I. Tayasu, & K. Koba (Eds.), *Earth, Life, and Isotopes* (pp. 339–353). Japan: Kyoto.

Pagani, M., Arthur, M. A., & Freeman, K. H. (1999). Miocene evolution of atmospheric carbon dioxide. *Paleoceanography*, *14*(3), 273–292. https://doi.org/10.1029/1999PA900006

Pound, M. J., Haywood, A. M., Salzmann, U., & Riding, J. B. (2012). Global vegetation dynamics and latitudinal temperature gradients during the Mid to Late Miocene (15.97-5.33Ma). *Earth-Science Reviews*, *112*(1–2), 1–22. https://doi.org/10.1016/j.earscirev.2012.02.005

Prell, W. L., & Van Campo, E. (1986). Coherent response of Arabian Sea upwelling and pollen transport to late Quaternary monsoonal winds. *Nature*, *323*(6088), 526–528. https://doi.org/10.1038/323526a0

Raymond, P. A., & Bauer, J. E. (2001). Use of ^{14}C and ^{13}C natural abundances for evaluating riverine, estuarine, and coastal DOC and POC sources and cycling: A review and synthesis. *Organic Geochemistry*, *32*(4), 469–485. https://doi.org/10.1016/S0146-6380(00)00190-X

Reuter, M., Piller, W. E., Brandano, M., & Harzhauser, M. (2013). Correlating Mediterranean shallow water deposits with global Oligocene-Miocene stratigraphy and oceanic events. *Global and Planetary Change*, *111*, 226–236. https://doi.org/10.1016/j.gloplacha.2013.09.018

Reuter, M., Piller, W. E., Harzhauser, M., Mandic, O., Berning, B., Rögl, F., et al. (2009). The Oligo-/Miocene Qom formation (Iran): Evidence for an early Burdigalian restriction of the Tethyan Seaway and closure of its Iranian gateways. *International Journal of Earth Sciences*, *98*(3), 627–650. https://doi.org/10.1007/s00531-007-0269-9

Rodriguez, M., Chamot-Rooke, N., Huchon, P., Fournier, M., & Delescluse, M. (2014). The Owen Ridge uplift in the Arabian Sea: Implications for the sedimentary record of Indian monsoon in Late Miocene. *Earth and Planetary Science Letters*, *394*(May 2014), 1–12. https://doi.org/10.1016/j.epsl.2014.03.011

Rögl, V. F. (1998). Palaeogeographic considerations for Mediterranean and paratethys seaways (Oligocene to Miocene). *Annalen Des Naturhistorischen Museums in Wien*, *99A*(April), 279–310.

Rohling, E. J., Marino, G., & Grant, K. M. (2015). Mediterranean climate and oceanography, and the periodic development of anoxic events (sapropels). *Earth-Science Reviews*, *143*, 62–97. https://doi.org/10.1016/j.earscirev.2015.01.008

Rommerskirchen, F., Condon, T., Mollenhauer, G., Dupont, L., & Schefuss, E. (2011). Miocene to Pliocene development of surface and subsurface temperatures in the Benguela Current system. *Paleoceanography*, *26*(3), n/a–n/a. https://doi.org/10.1029/2010PA002074

Schmitz, B., Charisi, S. D., Thompson, E. I., & Speijer, R. P. (1997). Barium, SiO2 (Excess), and P2O5 as proxies of biological productivity in the Middle East during the Palaeocene and the Latest Palaeocene benthic extinction event. *Terra Nova*, *9*(2), 95–99. https://doi.org/10.1111/j.1365-3121.1997.tb00011.x

Schott, F. A., Xie, S.-P., & McCreary, J. P. (2009). Indian Ocean circulation and climate variability. *Reviews of Geophysics*, *47*(1), RG1002. https://doi.org/10.1029/2007RG000245

Shevenell, A. E. (2004). Middle Miocene Southern Ocean cooling and Antarctic cryosphere expansion. *Science*, *305*(5691), 1766–1770. https://doi.org/10.1126/science.1100061

Shimmield, G. B. (1992). Can sediment geochemistry record changes in coastal upwelling palaeoproductivity? Evidence from northwest Africa and the Arabian Sea. *Geological Society, London, Special Publications*, *64*(1), 29–46. https://doi.org/10.1144/GSL.SP.1992.064.01.03

Shipboard Scientific Party (1974). Site 222. In R. B. Whitmarsh, O. E. Weser, & D. Ross (Eds.), *Initial reports of the deep sea drilling project* (Vol. 23, pp. 211–290). College Station, TX. https://doi.org/10.2973/dsdp.proc.23.106.1974

Shipboard Scientific Party (1989). Site 722. In *Proceedings of the ocean drilling program—Initial reports* (Vol. 117, pp. 441–446). College Station, TX. https://doi.org/10.2973/odp.proc.ir.117.107.1989

Sirocko, F., Garbe-Schonberg, D., McIntyre, A., & Molfino, B. (1996). Teleconnections between the subtropical monsoons and high-latitude climates during the last deglaciation. *Science*, *272*(5261), 526–529. https://doi.org/10.1126/science.272.5261.526

Smart, C. W., Thomas, E., & Ramsay, A. T. S. (2007). Middle-late Miocene benthic foraminifera in a western equatorial Indian Ocean depth transect: Paleoceanographic implications. *Palaeogeography, Palaeoclimatology, Palaeoecology*, *247*(3–4), 402–420. https://doi.org/10.1016/j.palaeo.2006.11.003

Stramma, L., Johnson, G. C., Sprintall, J., & Mohrholz, V. (2008). Expanding oxygen-minimum zones in the Tropical Oceans. *Science*, *320*(5876), 655–658. https://doi.org/10.1126/science.1153847

Tachikawa, K., Vidal, L., Cornuault, M., Garcia, M., Pothin, A., Sonzogni, C., et al. (2015). Eastern Mediterranean Sea circulation inferred from the conditions of S1 sapropel deposition. *Climate of the Past*, *11*(6), 855–867. https://doi.org/10.5194/cp-11-855-2015

Tayasu, I., Hirasawa, R., Ogawa, N. O., Ohkouchi, N., & Yamada, K. (2011). New organic reference materials for carbon- and nitrogen-stable isotope ratio measurements provided by Center for Ecological Research, Kyoto University, and Institute of Biogeosciences, Japan Agency for Marine-Earth Science and Technology. *Limnology*, *12*(3), 261–266. https://doi.org/10.1007/s10201-011-0345-5

Tian, J., Ma, W., Lyle, M. W., & Shackford, J. K. (2014). Synchronous mid-Miocene upper and deep oceanic $\delta^{13}C$ changes in the east equatorial Pacific linked to ocean cooling and ice sheet expansion. *Earth and Planetary Science Letters*, *406*, 72–80. https://doi.org/10.1016/j.epsl.2014.09.013

Tripathi, S., Tiwari, M., Lee, J., Khim, B.-K., Pandey, D. K., Clift, P. D., et al. (2017). First evidence of denitrification vis-à-vis monsoon in the Arabian Sea since Late Miocene. *Scientific Reports*, *7*(1), 43056. https://doi.org/10.1038/srep43056

Tyson, R. V. (1995). *Sedimentary Organic Matter*. Dordrecht: Springer Netherlands. https://doi.org/10.1007/978-94-011-0739-6

Verducci, M., Foresi, L. M., Scott, G. H., Sprovieri, M., Lirer, F., & Pelosi, N. (2009). The Middle Miocene climatic transition in the Southern Ocean: Evidence of paleoclimatic and hydrographic changes at Kerguelen plateau from planktonic foraminifers and stable isotopes. *Palaeogeography, Palaeoclimatology, Palaeoecology*, *280*(3–4), 371–386. https://doi.org/10.1016/j.palaeo.2009.06.024

Wade, B. S., Pearson, P. N., Berggren, W. A., & Pälike, H. (2011). Review and revision of Cenozoic tropical planktonic foraminiferal biostratigraphy and calibration to the geomagnetic polarity and astronomical time scale. *Earth-Science Reviews*, *104*(1–3), 111–142. https://doi.org/10.1016/j.earscirev.2010.09.003

Ward, B. B., Devol, A. H., Rich, J. J., Chang, B. X., Bulow, S. E., Naik, H., et al. (2009). Denitrification as the dominant nitrogen loss process in the Arabian Sea. *Nature*, *461*(7260), 78–81. https://doi.org/10.1038/nature08276

Wu, R. (2017). Relationship between Indian and East Asian summer rainfall variations. *Advances in Atmospheric Sciences*, *34*(1), 4–15. https://doi.org/10.1007/s00376-016-6216-6

Xue, F., Wang, H., & He, J. (2004). Interannual variability of Mascarene high and Australian high and their influences on East Asian summer monsoon. *Journal of the Meteorological Society of Japan*, *82*(4), 1173–1186. https://doi.org/10.2151/jmsj.2004.1173

Young, J. (1990). Size variation of Neogene Reticulofenestra coccoliths from Indian Ocean DSDP cores. *Journal of Micropalaeontology*, *9*(1), 71–85. https://doi.org/10.1144/jm.9.1.71

Zhang, Z., Ramstein, G., Schuster, M., Li, C., Contoux, C., & Yan, Q. (2014). Aridification of the Sahara desert caused by Tethys Sea shrinkage during the Late Miocene. *Nature*, *513*(7518), 401–404. https://doi.org/10.1038/nature13705

Zhisheng, A., Clemens, S. C., Shen, J., Qiang, X., Jin, Z., Sun, Y., et al. (2011). Glacial-interglacial Indian summer monsoon dynamics. *Science*, *333*(6043), 719–723. https://doi.org/10.1126/science.1203752

Zhongshi, Z., Huijun, W., Zhengtang, G., & Dabang, J. (2007). Impacts of tectonic changes on the reorganization of the Cenozoic paleoclimatic patterns in China. *Earth and Planetary Science Letters*, *257*(3–4), 622–634. https://doi.org/10.1016/j.epsl.2007.03.024

Zhuang, G., Pagani, M., & Zhang, Y. G. (2017). Monsoonal upwelling in the western Arabian Sea since the middle Miocene. *Geology*, *45*(7), 655–658. https://doi.org/10.1130/G39013.1